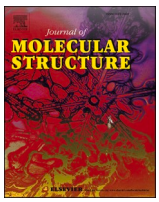
Journal of Molecular Structure 1321 (2025) 139921



Contents lists available at ScienceDirect

Journal of Molecular Structure

journal homepage: www.elsevier.com/locate/molstr



Synthesis and photoluminescence properties of Ce^{3+}/Tb^{3+} and Eu^{3+} ions doped $GdB_3O_6/Ca_{10}(PO_4)_6(OH)_2$ Core/Shell particles as well as its cytotoxicity against colon cancer cells

Mehmet Burak UZUN [a], İsmail GUDERER [b], Sreeparna BANERJEE [b], Ayşen YILMAZ [a,c,*]

[a] Department of Chemistry, Middle East Technical University, Ankara, Turkiye
[b] Department of Biological Sciences, Middle East Technical University, Ankara, Turkiye
[c] Department of Micro and Nanotechnology, Middle East Technical University, Ankara, Turkiye

ARTICLE INFO

Keywords:
Borates
Core/shell
Drug delivery
Real-time monitoring
Hydroxyapatite

ABSTRACT

In this study, Ce^{3+}/Tb^{3+} co-doped, Eu^{3+} doped GdB_3O_6 phosphor particles were synthesized by sol-gel method, coated with hydroxyapatite (HAP) and loaded with doxorubicin. Different chelating agents and surfactants (Cetyltrimethylammonium bromide (CTAB), citric acid, glycine, ethylenediaminetetraacetic acid (EDTA) and tartaric acid) were used in the synthesis in order to see their effect on the structure. While single phase Gadolinium triborate, GdB_3O_6 was obtained by using CTAB in precursor solution in the synthesis and Gadolinium orthoborate, $GdBO_3$ produced when EDTA was used in precursor solution. Other organic molecules added to precursor solution produced mixtures of both phases. The highest photoluminescence intensity was obtained in the $Gd_{0.95}Ce_{0.025}Tb_{0.025}B_3O_6$ and $Gd_{0.825}Eu_{0.175}B_3O_6$. In order to increase the drug loading efficiency, The $Gd_{0.825}Eu_{0.175}B_3O_6$ core was coated with Calcium hydroxyapatite, HAP. The core had an average size of 458.65 nm which increased to 616.85 nm after coating as seen with dynamic light scattering (DLS). $Gd_{0.825}Eu_{0.175}B_3O_6$@HAP particles were loaded with 7.82 % ± 0.80 wt doxorubicin and the release was studied at 37 °C in pH 7.4 phosphate-buffered saline (PBS) and pH 5.5 acetate buffer solutions. The total number of moles of drug released versus luminescence intensity was measured during the release studies and real-time imaging studies were carried out. Finally, cytotoxicity experiments were performed on HCT-116 colon cancer cells.

1. Introduction

The most used boron products in the industry are borates. Borates are an important part of solid-state chemistry due to their functionality and have attracted the attention of researchers due to their complex structure. Since there are many modes of B-O bonding and their association with metals, borates have a wide range of applications as optical materials [1]. Gadolinium can be used in magnetic and optical imaging strategies. Due to the paramagnetic properties of the Gd^{3+} ion, it can be used as a magnetic resonance imaging agent, while its optical properties allow it to be used in optical imaging [2]. Gadolinium contrast agents decrease the longitudinal relaxation time and can provide brighter and better-focused magnetic resonance imaging images due to their high magnetic moment and long electron spin relaxation time [3]. Because of its high first excitation transition, rare earth elements can be doped into the Gadolinium compounds as host, allowing them to energy transfer mechanisms or receive the desired emission [4]. There are a few applicable Gadolinium borates available for host material, such as Gadolinium orthoborate, $GdBO_3$ [5], Gadolinium triborate or metaborate GdB_3O_6 [6], and Gadolinium oxo-borate $Gd_2B_4O_9$ [7].

The sol-gel process is one of the most important methods developed for nano-sized borates. This process consists of hydrolysis and condensation steps. Briefly, an alkoxide stable solution is formed, called sol and a gel network is formed by polycondensation. The process is completed by dehydration and decomposition of the gel. Pechini has reported a modified sol-gel method for metal elements that are difficult to hydrolyze [8]. Complex structures formed when chelating agents bind with polyalcohols, initiating the esterification reaction. This esterification causes the solution to form a gel over time. After burning the organic molecules in the gel by calcination to produce powder product, agglomerated nano- or micron-sized particles are usually obtained [9].

Hydroxyapatite is an inorganic compound with the formula of

* Corresponding author.
E-mail address: ayseny@metu.edu.tr (A. YILMAZ).

https://doi.org/10.1016/j.molstruc.2024.139921
Received 7 February 2024; Received in revised form 5 August 2024; Accepted 2 September 2024
Available online 10 September 2024
0022-2860/© 2024 Elsevier B.V. All rights are reserved, including those for text and data mining, AI training, and similar technologies.

$Ca_{10}(PO_4)_6(OH)_2$ and is the most abundant mineral in bones and teeth. For this reason, it is used in osteoinductive and regeneration studies. In addition to these properties, hydroxyapatite is also widely used in drug-delivery systems. Being a biocompatible material allows it to overcome biological barriers. This drug delivery system can transport vitamins, hormones, antibiotics and anticancer drugs [10]. In drug delivery systems, different mechanisms can be used to load drugs into the carrier. These include sorption, chemical bonding or mechanical aspects. In the strategies developed in recent years, intermolecular forces can be used as a strategy between the drug and the carrier. With a basic strategy, the carrier and the drug can be attached by this method and the sorption mechanism is activated. Hydroxyapatite interacts with the drug as an active site with the -OH groups in its structure and the drug is loaded onto the hydroxyapatite [11].

Recently, inorganic nanocarriers with fluorescent properties have been investigated by researchers to monitor drug loading and release properties. Drug monitoring is important to arrange dosage to reduce of side effects of drug such as toxicity, and damage to the immune system. Moreover, fluorescent imaging is a low-cost, highly selective, sensitive, and non-destructive method, which makes it easier to use. For these reasons, fluorescent trackers have attracted the attention of researchers for theranostics and have become a good candidate for real-time monitoring in drug delivery systems [12-15].

This study aimed to develop luminescent nanoparticles that can perform real-time monitoring as well as deliver drugs. Ce^{3+}/Tb^{3+} co-doped GdB_3O_6 with different chelating agents and surfactant were synthesized and characterized to see the effect on the crystal structure and photoluminescence intensity in $Gd_{0.95}Ce_{0.025}Tb_{0.025}B_3O_6$ particles. Eu^{3+} doped GdB_3O_6 and $GdBO_3$ were synthesized and characterized with different dopant ratios to see concentration quenching and how dopant ratio affects the crystal structure. $Gd_{0.825}Eu_{0.175}B_3O_6$ particles were coated with hydroxyapatite to increase the drug loading capacity and real-time monitoring studies were performed using the optical properties of the particles.

2. Experimental procedure

2.1. Synthesis

2.1.1. Synthesis of GdB_3O_6 particles

The oxides were converted into nitrate salts with nitric acid (65 %, Merck) to increase their solubility's in water. A stoichiometric amount of nitric acid was added to the rare earth oxides and stirred at 80 °C. The nitrate salts were added to 0.80 g H_3BO_3 (99.5 %, Merck), cationic surfactant CTAB (or chelating agents (EDTA, citric acid, glycine and tartaric acid) and water prepared in a stoichiometric ratio. 200 mL of solution was stirred at 80 °C until the dark resin was obtained. Ce^{3+}/Tb^{3+} codoped GdB_3O_6 synthesis was calcinated at 900 °C for all different chelating agents and surfactant. For instance, synthesis of $Gd_{0.95}Ce_{0.025}Tb_{0.025}$ was started with 0.59 g Gd_2O_3 (99.9 %, Acros Organics), 0.022 g $Ce_2(CO_3)_3$ (99.9 %, Aldrich), and 0.036 g Tb_4O_7 (%99.9, Aldrich). Rare earth oxides were nitrated with 10 mL of nitric acid. 0.80 g H_3BO_3, 0.51 g CTAB (>98 %, Sigma) stirred with 200 mL water. When the solution was heated to 80 °C. Rare earth nitrates were added to the solution. After the dark resin was obtained while stirring at 80 °C. The resin was calcined at 900 °C for 6 h.

2.1.2. Calcium hydroxyapatite coating

Calcium Hydroxyphosphate was synthesized on the core as a shell to improve drug loading capacity. The wet precipitation method was used to synthesize hydroxyapatite. $Ca(NO_3)_2{\cdot}4H_2O$ (Sigma) and $(NH_4)_2HPO_4$ (Merck) and NH_4OH (Merck) were used as precursors.

First, 0.5 gs of synthesized particles were dispersed into 0.06 M $Ca(NO_3)_2{\cdot}4H_2O$ solution and stirred for 1 hour. Then 0.07 M $(NH_4)_2HPO_4$ solution was slowly added into the solution and pH was kept constant with NH_4OH at pH 9. After the particles were mixed for 2 h, then the coating process was removed by centrifuge, washed by de-ionized water and calcined at 600° for 2 h.

2.1.3. Doxorubicin loading and release

Doxorubicin hydrochloride was used as a model drug. In order to investigate drug storage and release, the prepared 1000 ppm (1 mg/mL) doxorubicin hydrochloride solution was diluted in phosphate pH 7.4, acetate at pH 5.5 and water at certain concentrations and calibration curves were prepared according to the highest absorbance value of doxorubicin hydrochloride solution at 480 nm.

For drug loading, 10 mg of the particles was added into 2 mL of 1000 ppm doxorubicin hydrochloride solution. The prepared suspension was first stirred in a sonicator for 30 min and then stirred in the dark and inert atmosphere for 24 h. The suspension was then separated by centrifugation at 6000 rpm for 10 min. For release of the drug, drug-loaded particles were taken into 1 mL acetate (pH 5.5) or phosphate (pH 7.4) buffer solutions, mixed at 150 rpm in a 37 °C incubator to simulate physiological temperature. 300 μL of the suspension was sampled at 30 min 1, 2, 3, 4, 5, 6 and 24 h, divided into three and the absorbance of each 100 μL sample was measured after the addition of 300 μL of fresh buffer solution onto it. The average of three measurements taken based on the maximum absorbance values at 480 nm. The release processes were determined over total moles of drug. Since the number of moles of drug loaded was known from the previous process, the total moles was calculated at each step. Firstly, the absorbance values obtained were substituted into the relevant calibration curves and the concentration of the released drug was calculated.

2.1.4. Cell culture

The colorectal cancer cell line HCT-116 was purchased from ATCC (American Type Culture Collection). HCT-116 cells were cultured in RPMI (Roswell Park Memorial Institute Medium, Biological Industries) medium supplemented with l-glutamine (2 mmol/L), 1 % pen/strep solution and 10 % FBS (fetal bovine serum). For subculturing, the old medium was first removed, then the cells were washed with 1X PBS (phosphate buffered salt) and incubated with 0.25 % Trypsin-EDTA at 37 °C until the cells are detached from the growth surface (5–10 min). A complete medium with three times the amount of trypsin was used for trypsin inhibition. Cells were centrifuged at 2000 x *g* for 2 min and the supernatant was removed and the cells were suspended with appropriate amount of fresh medium and transferred to new growth flasks or plates. HCT116 cell line was grown in a humidified and sterile environment at 37 °C with 5 % CO_2. The cell lines were regularly tested for mycoplasma contamination by PCR and Plasmocin (Invivogen, USA) was added to the media to prevent mycoplasma contamination.

2.1.5. MTT analysis

The change in growth and viability of cells after treatment with nanoparticles was determined using MTT [3-(4,5-Dimethylthiazol-2-yl)−2,5-Diphenyltetrazolium bromide]. For the assay, cells were seeded in 96-well plates with 10,000 cells per well as recommended by the MTT protocol. One day after seeding the cells, nanoparticles were prepared by serial dilution method from 100 μg/mL to 12.5 μg/mL concentration of loaded doxorubicin and treated for 24 h. Free doxorubicin of the same concentration was used as a control. At the end of the treatment period, the media were replaced with fresh media containing MTT and incubated for 4 h. At the end of the incubation period, 1 % SDS - 0.01 M HCl solution was added to each well to dissolve the formazan crystals formed. The plates were incubated for 16 h and the absorbance at 570 nm wavelength was measured with a spectrophotometer (Multiskan GO; Thermo Fisher Scientific, USA). For the statistical analysis, the absorbance of wells containing only medium and MTT (blank) was subtracted from all other data and the resulting data was normalized to the absorbance of untreated cells and presented as the growth rate (%).

2.2. Characterization

The crystal structures of metal ion-doped and undoped borate compounds were monitored by powder X-ray diffraction measurement. The powder X-ray pattern of each crystal structure of each compound is like a fingerprint of the crystal structure of the compound. The powder X-ray information is recorded in libraries and listed on JCPDS (Joint Committee of Powder Diffraction System) cards. X-ray diffraction patterns were measured on a Rigaku Miniflex X-Ray Diffractometer. Cu Kα(30 kV, 15 mA, λ = 1.54Å) was used as the x-ray source. For measurements taken between 5° and 90°, the goniometer was set to rotate 2° per minute. Infrared spectroscopy was used to determine the vibrational modes. The measurements were performed using a Nicolet iS50 FTIR Spectrometer with an Attenuated total reflection cap and pellet and the measurements were studied at wavenumber in the range of 540–4000 cm^{-1}. A photoluminescence spectrometer was used to determine the optical properties. The measurements were carried out with Varian Cary Eclipse Fluorescence Spectrometer and Edinburgh Instruments FS5, excitation spectra were based on maximum emission and emission spectra were based on maximum excitation. Decay curve measurements were taken to calculate the optical extinction. In the handmade device, a 365 nm pulsed laser was used as a source. A photomultiplier tube (Oriel 70–680) was used as a detector. Measurements were taken after the nanoparticles were pelletized. To examine the morphological properties of the nanoparticles, images were taken at METU Central Laboratory: TEM images were taken with JEOL JEM 2100F STEM and a JEOL JEM 2100F Field Emission Gun at 120 kV. .QUANTA 400F Field Emission SEM device used for SEM images. For the determination of the elements on the surface of the obtained nanoparticles, JXA- 8230 electron probe microanalysis device was used in METU Central Laboratory. The size distribution of the synthesized particles was obtained by dynamic light scattering spectrophotometry. Zetasizer Nano ZS device was used for dynamic light scattering analysis. Zeta potential measurements were also performed on the same device and the phase plot and frequency values given by the device were followed to obtain accurate measurements, 0.1 M HCl (Sigma-Aldrich) and NaOH (Sigma-Aldrich) solutions were used to adjust pH. UV–VIS spectrometer was used to monitor drug loading and release profiles. The experiments were performed using Agilent Synergy H1 Hybrid Multi-Mode Reader, measurements were taken using 96 well plates.

3. Results and discussion

3.1. X-Ray diffraction pattern of Ce^{3+}/Tb^{3+} codoped GdB_3O_6 structure with different chelating agents and surfactant and hydroxy apatite coated GdB_3O_6

To improve the optical properties of phosphors, the advantageous features of the sol-gel process were utilized such as production of phase pure, smaller and monodispersed particle size and homogeneous distribution of dopant ions in the host. Sol–gel chemistry is the preparation of inorganic ceramics from solution through a transformation from liquid precursors to a sol and finally to a network structure called a 'gel' [16]. The formation of a sol occurs through hydrolysis and condensation of metal alkoxide precursors and a sol can be more generally defined as a colloidal suspension. In order to control structure and particle dimension of product templates or chelating agents can be used in sol formation: Cetyltrimethyl ammonium bromide (CTAB) is most commonly used amphiphilic copolymer in sol-gel synthesis: Inorganic material accumulates around this template in solution, which results in well-ordered structuring in the produced metal oxide. The other molecules used in sol-gel formation, EDTA, citric acid, tartaric acid and glycine are 'chelating agents'. Chelating agents change the hydrolysis equilibria of dissolved metals. By making hydrolysis considerably less favorable, the removal of solvent from many metal-chelate solutions results in homogeneous glassy solids or resins rather than precipitates. These can be heat treated to form powders or nanostructures of wide range of binary or ternary metal oxides. In our experiments, phase pure GdB_3O_6 was produced by using CTAB in precursor solution while EDTA usage produced $GdBO_3$. The other molecules produced mixtures of both compounds. In comparison between CTAB and EDTA, CTAB is better to change surface tension to prevent agglomeration of particles. In between EDTA, citric acid, tartaric acid and glycine the chelating capacity of EDTA is highest [17,18].Citric acid is a weak triprotic acid with three carboxylic acid groups that able to dissociate. In typical synthesis, aqueous metal nitrates are mixed with citric acid and resulting solution heated to form a viscous solution or gel. The homogeneity and stability of metal citrate solutions can depend strongly on pH [19].Tartaric acid is diprotic acid and glycine is monoprotic aminoacid. Glycine is a common chelator and 'fuel' and has a lower ignition temperature of combustion than citrate. Glycine–nitrate mixtures burn quickly, releasing gases and forming 'fluffy' powders [20]. As a result, the production of phase pure $GdBO_3$ depends on high chelating capacity of EDTA in sol-gel process. X-Ray diffraction analysis was carried out to analyze the crystal structure of Ce^{3+}/Tb^{3+} doped CTAB and EDTA synthesized GdB_3O_6 and $GdBO_3$ nanoparticles (Fig. 1). The GdB_3O_6 structure obtained with tartaric acid, glycine and citric acid and matched with the corresponding card data belonging to $GdBO_3$ were signed. The recorded diffraction peaks of Ce^{3+}/Tb^{3+} doped GdB_3O_6 with synthesized CTAB, nanoparticles were in agreement with JCPDS card number 70–2239. It was determined that gadolinium triborate had a monoclinic crystal system and a C2/c space group. The lattice parameters were $a = 9.83$ Å $b = 8.15$ Å $c = 6.31$ Å and α=90° β=126.83° and γ=90°. Ce^{3+} ion, Tb^{3+} ion, and Gd^{3+} ion radii are 102pm, 92.3pm, and 93.8pm in 6 coordinates respectively. Due to the contraction of radii provided by lanthanides, ions that doped the structure could substitute the crystal structure with Gd^{3+} ions. CTAB is cationic surfactant that can increase the number of ions in solution. In the experiments with CTAB, a pH of 6.0 was determined. Thus, pH is an important factor in boric acid hydrolysis in the triborate structure obtained in sol-gel media. The GdB_3O_6 particle was successfully synthesized with CTAB in a single phase without formation of other borate compounds. Moreover, when the intensity values and full width at half maximum values of crystal structures with different chelating agents were compared, the highest intensity values and lowest full width at half maximum values were obtained with CTAB. Therefore, the highest crystalline and single-phase product was acquired with

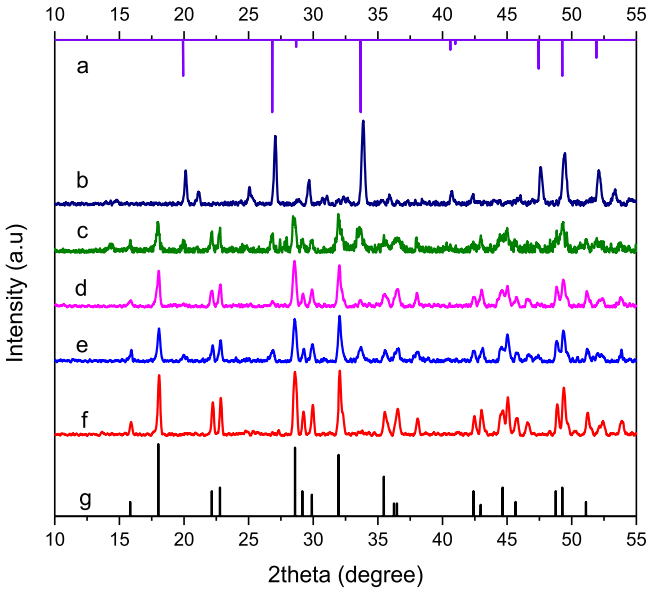


Fig. 1. X-Ray diffraction pattern of different chelating agents and surfactant synthesized borate structures a) $GdBO_3$ (JCPDS 13 – 0483), b) EDTA, c) tartaric acid, d) glycine, e) citric acid, f) CTAB, g) GdB_3O_6 (JCPDS 70 – 2239).

CTAB.

3.2. X-Ray diffraction patterns of Eu^{3+} doped GdB_3O_6 and $GdBO_3$

In order to compare structural and optical performance differences of both borate compounds Europium doped Gadolinium triborate and orthoborate were synthesized with changing concentrations of Eu content: X-Ray diffraction pattern of Eu^{3+} doped GdB_3O_6 up to 17.5 % mole concentrations of Eu^{3+} in GdB_3O_6 are shown in Fig. 2a. All data were compared with the JCPDS 70–2239 card and found to be compatible. In X-Ray analysis, the 2θ position can vary slightly with size, but it is difficult to distinguish these difference since ion sizes are very close to each other due to lanthanide contraction.

XRD analysis was also carried out to analyze the crystal structure of Eu^{3+} doped $GdBO_3$ particles synthesized with EDTA. The effect of Europium doping on the structure was examined. Eu^{3+} doping up to 20 % are shown in Fig. 2b. Eu^{3+} doped $GdBO_3$ nanoparticles were compared with the JCPDS 13–0483 card and found to be compatible. $GdBO_3$ was determined to have a hexagonal crystal system and a $P6_3/mmc$ space group. Lattice parameters were $a = b = 3.829$ Å and $c = 8.89$ Å and α=β=90° γ=120°. Our analysis indicated that the structure was safe up to 17 % Eu^{3+} doping and 20 % Eu^{3+} doping formed $EuBO_3$ which were marked. $EuBO_3$ has lattice parameters $a = b = 3.845$ Å and $c = 8.94$ Å and α=β=90° γ=120° with hexagonal crystal system which are very close to parameters of $GdBO_3$. The increase in the amount of Europium could change the crystal structure. Schott et al evaluated $EuBO_3$ complexes in aqueous solutions and observed the formation of borates in aqueous solutions with Europium, which can be attributed to the appearance of the Europium phase at increasing concentrations [21]. In addition, under high temperature, excess Eu^{3+} ion can form complexes with borate, which explains the emergence of these phases.

XRD analysis carried out after hydroxyapatite coating of Eu^{3+} doped GdB_3O_6 indicated that most of the diffraction peaks came from GdB_3O_6 particles. The generated diffraction pattern was compared with the GdB_3O_6 JCPDS card (Fig. 3). Since Gadolinium is a heavier element than calcium and GdB_3O_6 has a higher crystallinity when compared with hydroxyapatite, most of the diffractions are thought to come from the core which contained $Gd_{0.825}Eu_{0.175}B_3O_6$.

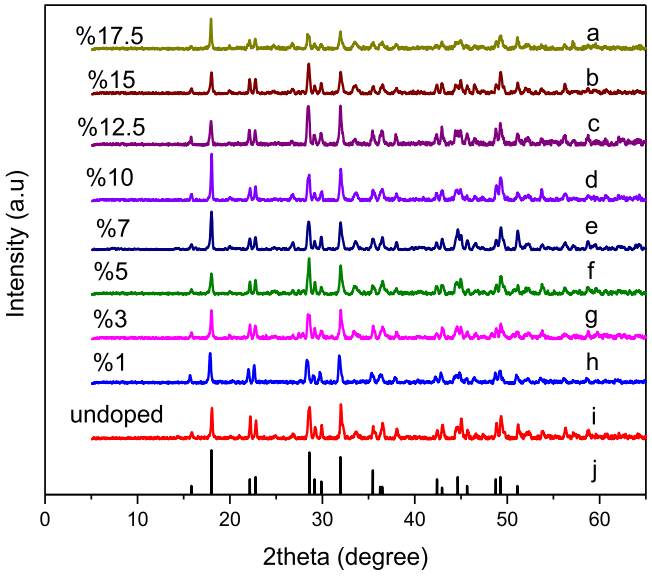


Fig. 2a. X-Ray diffraction pattern of Eu^{3+} doped GdB_3O_6 structure a) $Gd_{0.825}Eu_{0.175}B_3O_6$, b) $Gd_{0.85}Eu_{0.15}B_3O_6$, c) $Gd_{0.875}Eu_{0.125}B_3O_6$, d) $Gd_{0.90}Eu_{0.10}B_3O_6$, e) $Gd_{0.93}Eu_{0.07}B_3O_6$, f) $Gd_{0.95}Eu_{0.05}B_3O_6$, g) $Gd_{0.97}Eu_{0.03}B_3O_6$, h) $Gd_{0.99}Eu_{0.01}B_3O_6$, i) undoped GdB_3O_6 and j) GdB_3O_6 (JCPDS 70–2239).

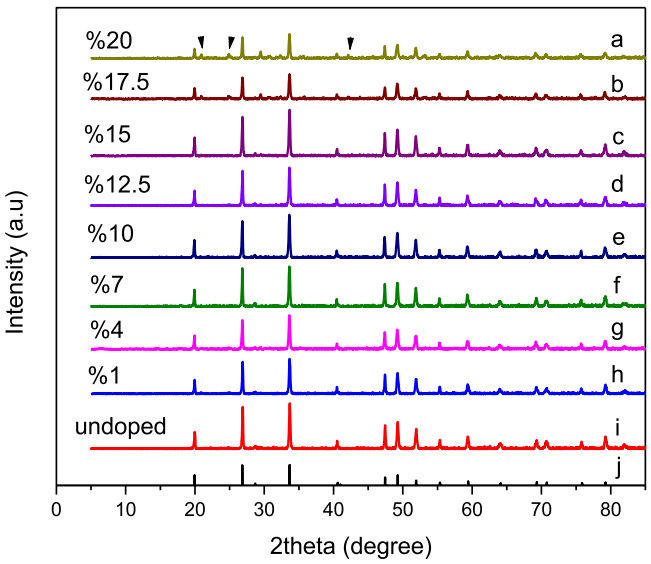


Fig. 2b. X-Ray diffraction patterns of Eu^{3+} doped $GdBO_3$ structure a) $Gd_{0.80}Eu_{0.20}BO_3$, b) $Gd_{0.825}Eu_{0.175}BO_3$, c) $Gd_{0.85}Eu_{0.15}BO_3$, d) $Gd_{0.875}Eu_{0.125}BO_3$, e) $Gd_{0.90}Eu_{0.10}BO_3$, f) $Gd_{0.93}Eu_{0.07}BO_3$, g) $Gd_{0.96}Eu_{0.04}BO_3$, h) $Gd_{0.99}Eu_{0.01}BO_3$, i) undoped $GdBO_3$ and j) $GdBO_3$ (JCPDS 13–0483).

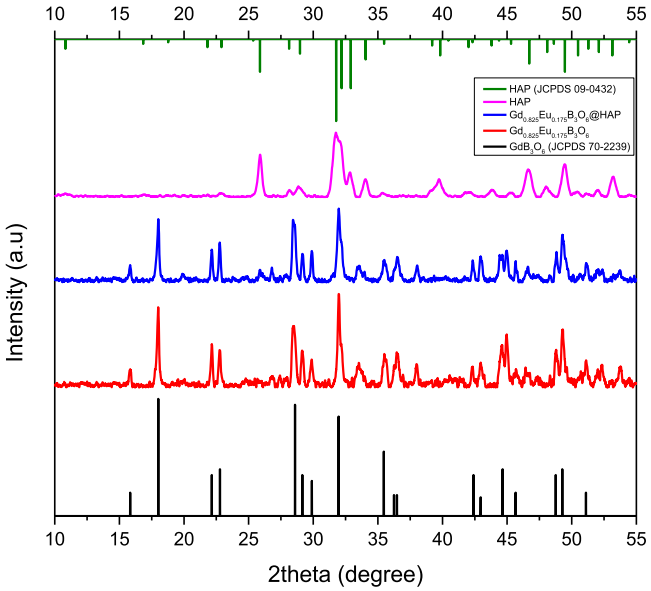


Fig. 3. X-Ray diffraction patterns a) $Gd_{0.825}Eu_{0.175}B_3O_6$@HAP, b) $Gd_{0.825}Eu_{0.175}B_3O_6$ and c) HAP (JCPDS 70–2239).

3.3. Photoluminescence measurements of Ce^{3+}/Tb^{3+} doped gdb_3o_6 and $gdbo_3$

The emission and excitation graph of Ce^{3+}/Tb^{3+} doped GdB_3O_6 particles synthesized with different chelating agents and surfactants is shown in Fig. 4. In addition to 5d → 4f transition of Ce^{3+} ions at 437 nm, the emission of Tb^{3+} ion was observed as $^5D_4 \rightarrow {}^7F_6$ transition at 480 nm, $^5D_4 \rightarrow {}^7F_5$ at 543 nm, $^5D_4 \rightarrow {}^7F_4$ at 590 nm and $^5D_4 \rightarrow {}^7F_3$ at 620 nm. Seraiche et al suggested that the highest luminescence intensity is achieved when the doped ion is uniformly distributed in the crystal cell [22]. A comparison of the different chelating agents and surfactant used in synthesis indicated that the highest luminescence intensity was obtained with CTAB. CTAB forms micelles in the solution in the synthesis and has a long carbon chain in its structure. These characteristics may enable CTAB to have the most uniform distribution that causes the

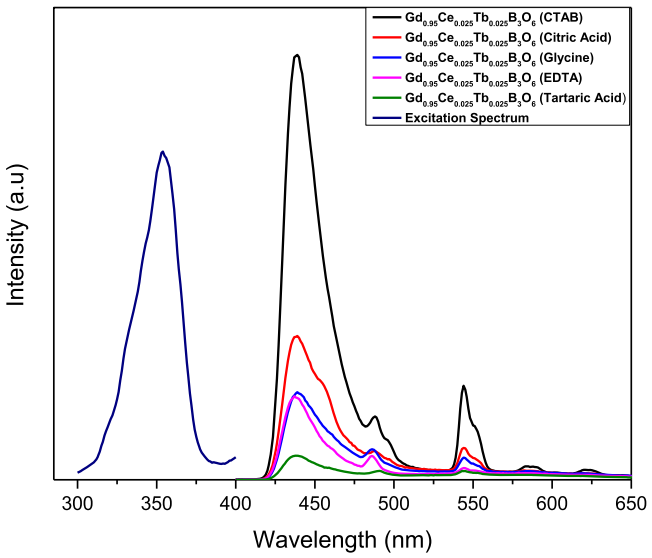


Fig. 4. Photoluminescence spectrum of $Gd_{0.95}Ce_{0.025}Tb_{0.025}B_3O_6$ with different chelating agents and surfactant

highest luminescence intensity. Another reason could be that the highest crystallinity in structure was obtained with CTAB since the highest intensity and lowest FWHM in the XRD pattern were acquired in the presence of CTAB. In addition, photoluminescence measurements were carried out with different amounts of CTAB used in the synthesis to observe effect of surfactant amount on luminescence intensity. Wang et al studied the effect of surfactants on the photoluminescence properties of ZnO films. These authors synthesized the films with different surfactants ratios and observed that the highest luminescence intensity was obtained with highest concentration of surfactant usage in synthesis because the crystallinity of product was increased by [23]. Same trend was observed in photoluminescence intensities of Ce^{3+}/Tb^{3+} doped GdB_3O_6 produced by using CTAB in sol-gel synthesis with increase in amount of CTAB in precursor solution.

3.4. Photoluminescence measurements of Eu^{3+} doped GdB_3O_6 and $GdBO_3$

After obtaining the highest luminescence intensity with CTAB in Ce^{3+}/Tb^{3+} doped GdB_3O_6, the same host was doped with Eu^{3+} ions. The excitation spectra for Eu^{3+} doped GdB_3O_6 particles were collected and the highest excitation values were determined. Thus, emission spectra were collected with excitation at 272 nm, 296 and 393 nm for transfer. Meng et al carried out optical studies on Eu^{3+} doped $Gd(BO_2)_3$ compound and reported an energy transfer from the Gd host to Eu at 272 nm. The $^8S_{7/2} \rightarrow {}^6I_{7/2}$ transition was attributed to this transfer. The optical properties were observed by exciting Eu at 393 nm due to the transition of $^7F_0 \rightarrow {}^5L_6$. These authors observed that Eu^{3+} doping did not cause concentration quenching, while the intensity increased as the amount of $Eu^{3+}$was increased [24]. The emission data collected by excitation at 393 nm were measured between 550 and 700 nm for both excitation and emission are given in (Fig. 5). The transition at 585 nm is referred to as the $^5D_0 \rightarrow {}^7F_1$ transition. Emission at 610 nm refers to emission $^5D_0 \rightarrow {}^7F_2$, emission at 650 nm to $^5D_0 \rightarrow {}^7F_3$ and emission at 700 nm to transition $^5D_0 \rightarrow {}^7F_4$. The reason why the emission to $^5D_0 \rightarrow {}^7F_1$ was higher than $^5D_0 \rightarrow {}^7F_2$ could be due to the magnetic dipole transition of $^5D_0 \rightarrow {}^7F_1$ emission and the electric dipole transition of $^5D_0 \rightarrow {}^7F_2$ emission [25]. Concentration quenching was not observed at increasing concentrations of the doped Eu^{3+} ion most likely because this phenomenon is usually seen with energy transfer [26]. Europium underwent a transition of $^7F_0 \rightarrow {}^5L_6$ at 394 nm; additionally, increasing the Europium concentration increased the intensity.

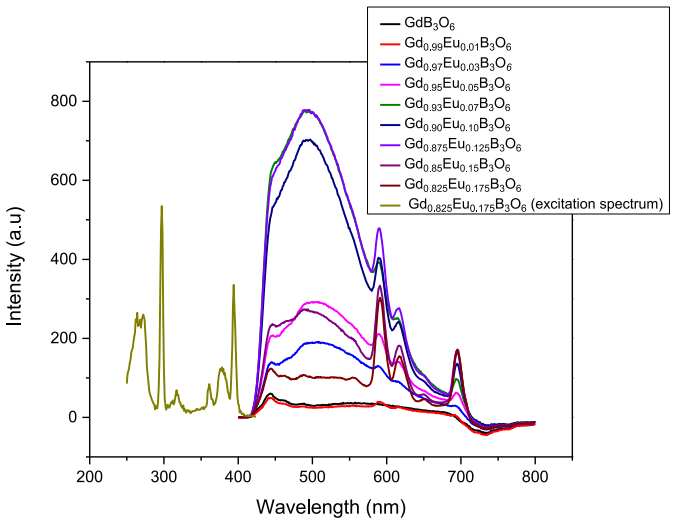


Fig. 5. Excitation and emission spectrum of $Gd_{0.825}Eu_{0.175}B_3O_6$.

The emission data of Eu^{3+} doped $GdBO_3$ was measured between 550 and 700 nm after excitation at 393 nm. The transition at 585 nm is referred to as the $^5D_0 \rightarrow {}^7F_1$ transition. Emission at 610 nm and 625 nm refers to emission $^5D_0 \rightarrow {}^7F_2$, emission at 650 nm to $^5D_0 \rightarrow {}^7F_3$ and no emission at 700 nm to transition $^5D_0 \rightarrow {}^7F_4$ was observed for the BO_3 structure. $^5D_0 \rightarrow {}^7F_2$ emissions split into two separate emissions lines due to the splitting of the crystal field. Emissions for Europium ions doped at different concentrations are presented in Fig. 6a. Concentration quenching was not observed as in the BO_3 structure at increasing europium concentration with the doped Eu^{3+} ion.

In line with the obtained photoluminescence results, $Gd_{0.825}Eu_{0.175}B_3O_6$ and $Gd_{0.80}Eu_{0.20}BO_3$ nanoparticles were compared depending on the intensity (Fig. 6b). The luminescence intensity was found to be higher in the Gadolinium triborate GdB_3O_6 compound than in the Gadolinium orthoborate $GdBO_3$. In addition, the transition at 700 nm could not be observed in the Gadolinium orthoborate. Using isolated BO_3, BO_4 and B_3O_6 groups, Rukang et al examined their electronic transition energies and UV absorption wavelengths. The results clearly show that, for isolated boron-oxygen anions, the first absorption corresponds to the electron transition from nonbridging oxygen to boron atoms. After introducing the alkali cations into boron oxide, the transition becomes a charge transfer transition from nonbridging oxygen to these cations. The cations lower the transition energy enormously and

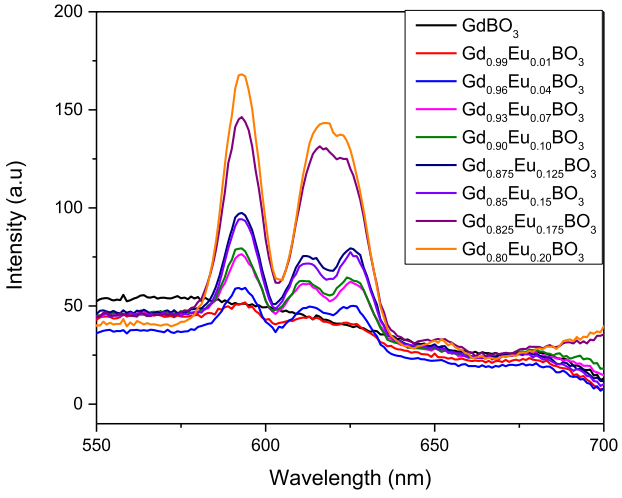


Fig. 6a. Emission spectrum of Eu^{3+} doped $GdBO_3$ structure with different doping concentrations.

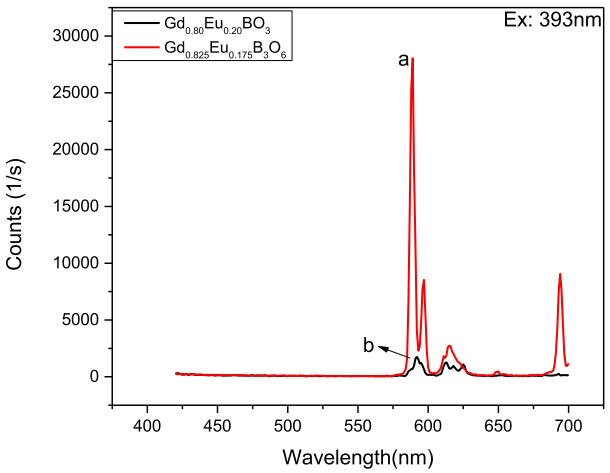


Fig. 6b. Comparison of a) $Gd_{0.825}Eu_{0.175}B_3O_6$ and b) $Gd_{0.80}Eu_{0.20}BO_3$ emission spectrum.

change the order of transition energies. Now the order becomes: E: B_3O_6 > BO_3 > BO_4. These authors reported that UV absorption was dominated by the bridging oxygen in the borate [27]. Accordingly, triborates are formed by combinations of BO_3 groups by oxygen sharing. Additionally, since their UV absorption is different, the triborate particles could absorb more and emit more making its intensity higher. The emission graph of the Eu^{3+} doped Gadolinium triborate at 394 nm and after coating with hydroxyapatite is shown in Fig. 6c. It is thought that the luminescence intensity decreases as a result of coating due to the differences of optical properties of core and shell.

3.5. Decay curve analysis

Decay lifetime measurements were carried out with a 365 nm pulsed laser excitation source. Since 585 nm had the highest intensity in the experiments with $Gd_{0.825}Eu_{0.175}B_3O_6$, the emission at 585 nm was used and the decay curves obtained were fit to double exponential decay functions in Fig. 7.

Where y_0 represents the emission intensity at $t = 0$, while y signifies the emission intensity at time x. The formulation involves using t_1 and t_2 to denote the fast and slow decay time components, respectively. The fast and slow decay lifetime components for $Gd_{0.825}Eu_{0.175}B_3O_6$ particles are calculated as 2.01 ms and 0.79 ms each. Similarly, for $Gd_{0.80}Eu_{0.20}BO_3$ particles, the fast and slow decay lifetime components

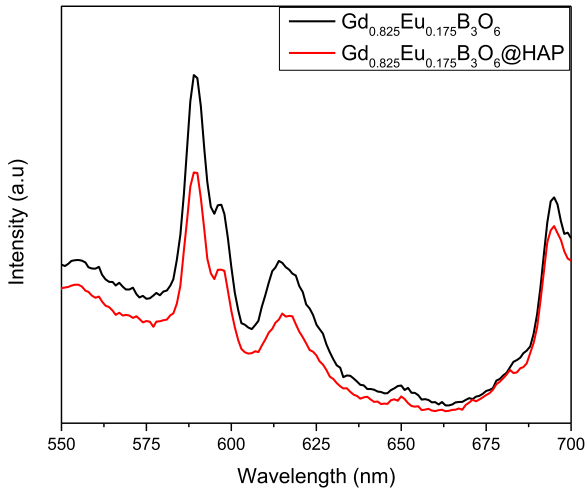


Fig. 6c. Comparison of emission spectrum of $Gd_{0.825}Eu_{0.175}B_3O_6$ (black) and after HAP coating (red)

are calculated as 1.5 x10^{-3} ms and 0.35 x10^{-3} ms, respectively. The intensity average lifetime is defined as,

$$y = y_0 + A_1 e(x/t_1) + A_2 e(x/t_2) tavg = \sum A_i t_i^2 \Big/ \sum A_i t_i$$

Where A_i is the fitting parameter and t_i is the lifetime component. The average decay lifetime is determined as 2.01 ms for $Gd_{0.825}Eu_{0.175}B_3O_6$ particles and 1.5 s for $Gd_{0.80}Eu_{0.20}BO_3$ particles. Further, the obtained average lifetime value was found comparable with the available literature [28-30]. The double exponential function suggests that the dopant ions are situated in two distinct environments.

3.6. FTIR spectra

Infrared analyses of $Gd_{0.825}Eu_{175}B_3O_6$, hydroxyapatite and hydroxyapatite-coated $Gd_{0.825}Eu_{175}B_3O_6$ structure are given in Fig. 8. The peaks of the coated triborate particles are also marked in the figure. It is known that the triborate anion group contains trigonal planar BO_3 and tetrahedral BO_4 groups together in structure. The peaks seen at 1100 and 1500 cm^{-1} are due to the modes of the BO_3 group. Peaks between 800 and 1100 cm^{-1} come from 4-fold boron bonding. The peaks at 812 and 673 cm^{-1} come from tetrahedral and trigonal planar peaks due to bending, respectively [28]. According to the analysis and literature review, 567 and 610 cm^{-1} peaks are due to the B-O bending mode, 675 and 812 cm^{-1} come from the trigonal BO_3 and tetrahedral BO_4 bending features, respectively, 1364 and 1464 cm^{-1} indicate BO_3 stretching. 3500 cm^{-1} indicates O—H stretching, while the peak at 1027 cm^{-1} belongs to the vibrational mode of the P-O group due to the hydroxyl apatite coating. Contrary to X-Ray analysis, vibrational patterns of the core and shell were observed very well in FTIR spectra. Another important point is that the O—H stretching mode was seen to distinguish hydroxyapatite from calcium phosphate, confirming the presence of hydroxyl groups in the structure and the successful coating of the particles [31–33].

3.7. Dynamic light scattering and zeta potential measurements

DLS results of GdB_3O_6 structures synthesized with CTAB and hydroxyapatite-coated are given in Fig. 9a. The size distribution by the number value of the GdB_3O_6 structure synthesized with CTAB was found to be 458.65 nm on average and 616.85 nm after HAP coating. This increase in particle size after coating suggests that the coating was successful. The grain size ranges from 400 to 800 nm, indicating their compatibility in the cell for potential bioimaging application [34]. In order to find differences of surface properties of core and core/shell particles the zeta potential measurements were performed at different pH values of particles dispersed in aqueous solutions. The electrostatic attraction, and thus flocculation behavior, is largely governed by solution pH due to its direct impact on surface charge. The pH at which the surface charge of a particle is zero is referred to as the point of zero charge (PZC). The core particles, $Gd_{0.825}Eu_{175}B_3O_6$ has a PZC near pH 2.30, HAP coated form of particles has a PZC near pH 3.04 and pure HAP has pH 3.14 value (Fig. 9b) [35].

3.8. Scanning and transmission electron microscopy

SEM images of GdB_3O_6 structures synthesized with CTAB and hydroxyapatite-coated were taken to examine their morphological properties (Fig. 10). SEM images indicate that the particles are agglomerated and exhibit irregular morphology prior to coating. While, after coating particles with hydroxyapatite SEM picture confirms formation of uniform granular and very well dispersed particles less than 700 nm size. It is very clear to understand that, coating with hydroxyapatite help to obtain more uniform morphological submicron sized particles.

To perform elemental analysis of the $Gd_{0.825}Eu_{0.175}B_3O_6$ particle

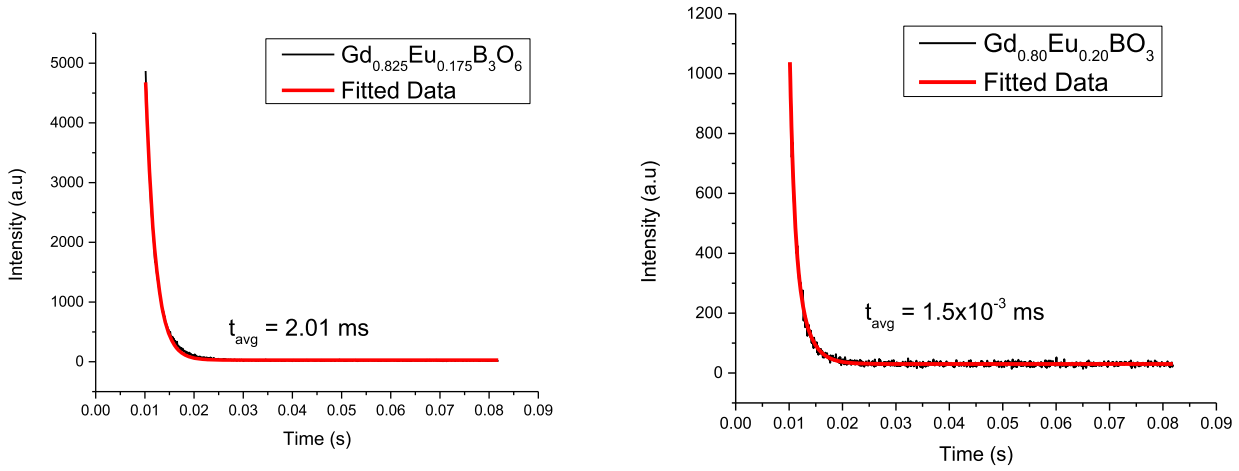


Fig. 7. Decay measurement for the $Gd_{0.825}Eu_{0.175}B_3O_6$ structure (left) and $Gd_{0.80}Eu_{0.20}BO_3$ (right).

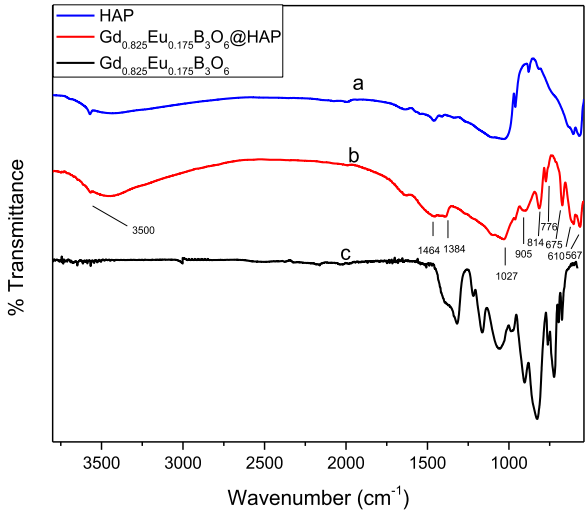


Fig. 8. FT-IR spectrum of a) hydroxyapatite, b) after hydroxyapatite coating c) $Gd_{0.825}Eu_{175}B_3O_6$.

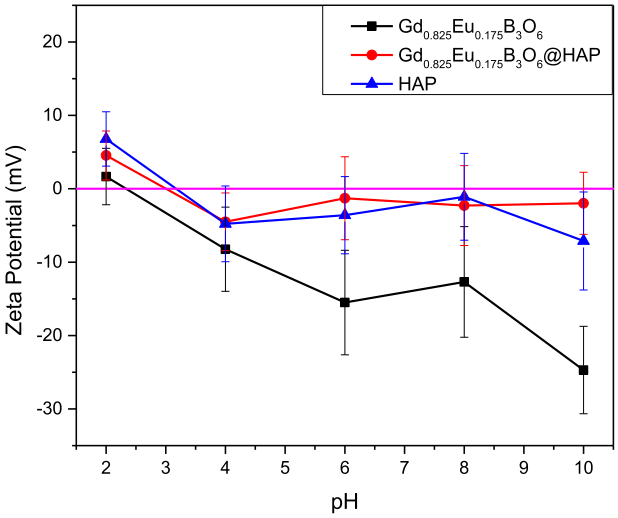


Fig. 9b. Comparison of charge as a function of pH and point of zero charges of $Gd_{0.825}Eu_{0.175}B_3O_6$ (black square), after hydroxyapatite coating (red circle) and calcium hydroxyapatite (blue triangle).

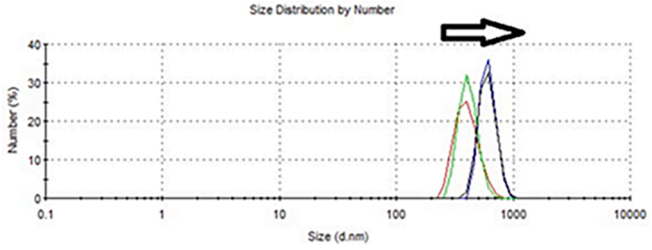


Fig. 9a. Dynamic Light Scattering before (left) and after (right) hydroxyapatite coating.

before and after hydroxyapatite coating and to characterize the hydroxyapatite coating, energy dispersive x-ray analysis was carried out (Fig. 11). The Ca/P mass ratio obtained after the coating was calculated as 1.45. Since the mass ratio of Hydroxyapatite itself is 1.67, the coating was considered to be successful [36].

Surface coating of nanomaterials with hydroxyapatite is common for biomedical applications of nanoparticles in order to improve adsorption capacity of drug and biocompatibility. In Fig. 12 TEM images of $Gd_{0.825}Eu_{0.175}B_3O_6$ and its hydroxyapatite coated form confirm that before coating the particles they had very dark contrast due to high atomic number of gadolinium. It is clearly observed that after the modification procedure with the hydroxyapatite precursor solutions the surface of particles was covered with smaller, rod like shape and pale Calcium hydroxyapatite crystals.

3.9. *Drug loading and drug release and real time monitoring*

A calibration curve was prepared prior to the loading of drugs. The $Gd_{0.825}Eu_{0.175}B_3O_6$ nanoparticle with high therapeutic potential was selected for drug loading. 10 mg of the particles was added into 2 mL of 1000 ppm doxorubicin hydrochloride solution. The prepared suspension was firstly mixed in a sonicator for 30 min and then stirred in the dark for 24 h. To prevent any oxidation of doxorubicin, drug loading was carried out in a nitrogen atmosphere. The suspension was then allowed to separate by centrifugation at 6000 rpm for 10 min. Intermolecular forces were considered to be the driving force for drug loading. Loading was carried out for 6 different samples to compare the release profiles at pH 7.4 and pH 5.5. Experiments were repeated three times on different days. Drug loading was determined from the supernatant obtained after centrifugation by measuring the absorbance value. To determine the amount of drug loaded, three different samples were taken from the supernatant and the average of the three was used. The amount loaded

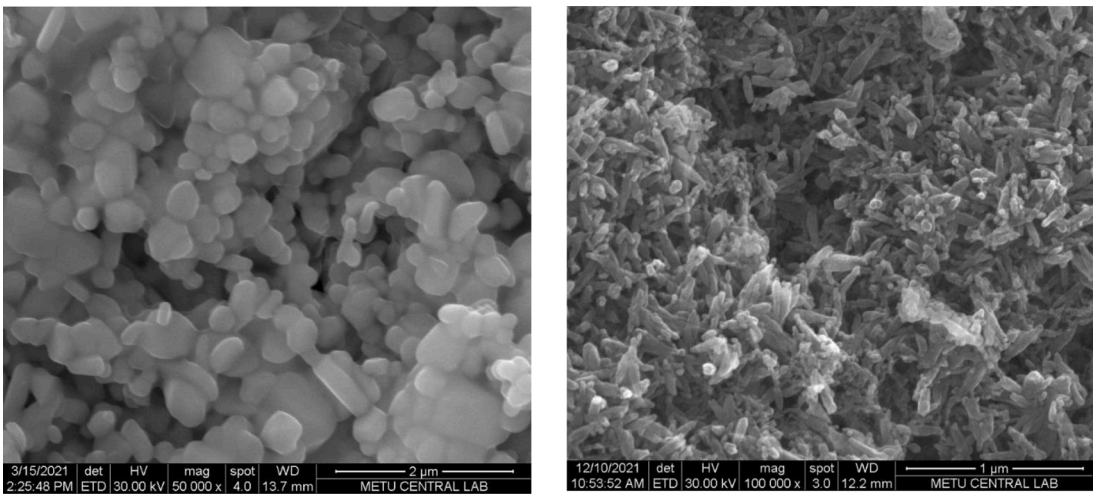


Fig. 10. SEM images of GdB_3O_6 before (left) and after (right) hydroxyapatite coating.

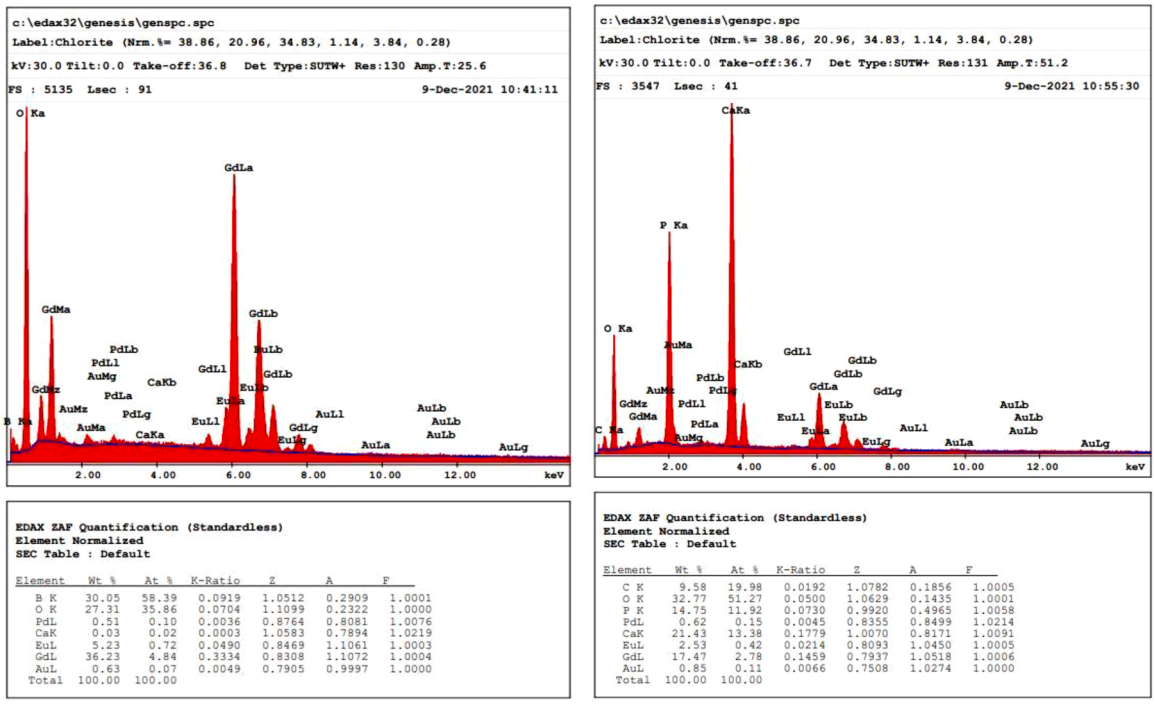


Fig. 11. EDX analysis before (left) and after (right) hydroxyapatite coating.

was determined from the calibration curve. The % loaded drug was calculated according to the equation below:

$$\%\ \text{Loaded Drug} = \frac{\text{Mass of drug loaded (g)}}{\text{Mass of nanoparticles(g)}}\ \text{x } 100$$

Accordingly, the absorbance values for samples 1, 2 and 3 were 1.16, 1.17 and 1.21, which corresponded to 0.73 mg, 0.71 mg, and 0.68 mg of doxorubicin, respectively, in the supernatant. The % loaded drug was calculated by subtracting the amount of drug in the supernatant from the initial amount of drug used. According to the results obtained, the weight percentage of the loaded drug was calculated as 7.82 % ± 0.80.

Drug release studies were performed in PBS buffer at pH 7.4 at a temperature of 37 °C to simulate physiological temperature. Firstly, the concentrations were calculated on the basis of absorbance values using the relevant calibration curve. For this, 300 µL of the sample was taken and 100 µL from this was placed in wells of a 96 well plate. Next, 300 µL of fresh PBS was added. Thus, the number of moles obtained for each time point was determined and the amount of drug loaded was calculated as % release per hour (Fig. 13(a)). The same experiments were carried out in acetate buffer at pH 5.5 under the same conditions. The tumor microenvironment is known to be more acidic. Most tumors utilize high levels of glucose through glycolysis (Warburg effect) releasing lactate and H^+ ions, which causes the pH to decrease [37]. We observed that 28 % of the loaded drug was released at pH 7.4 in 24 h, while about 40 % was released in at pH 5.5. Moreover, most of the release occurs as a burst in the first 2 h and the subsequent release happened more slowly in the following hours. The drug release from $Gd_{0.825}Eu_{0.175}B_3O_6$@HAP particles was also monitored by photoluminescence measurements at pH 7.4 (Fig. 13(b)). The drug-loaded particles were centrifuged and the photoluminescence of the supernatant was measured at an excitation wavelength of 394 and emission at 585 nm. An increase in intensity as the drug was released is expected and is in line with the literature [38].

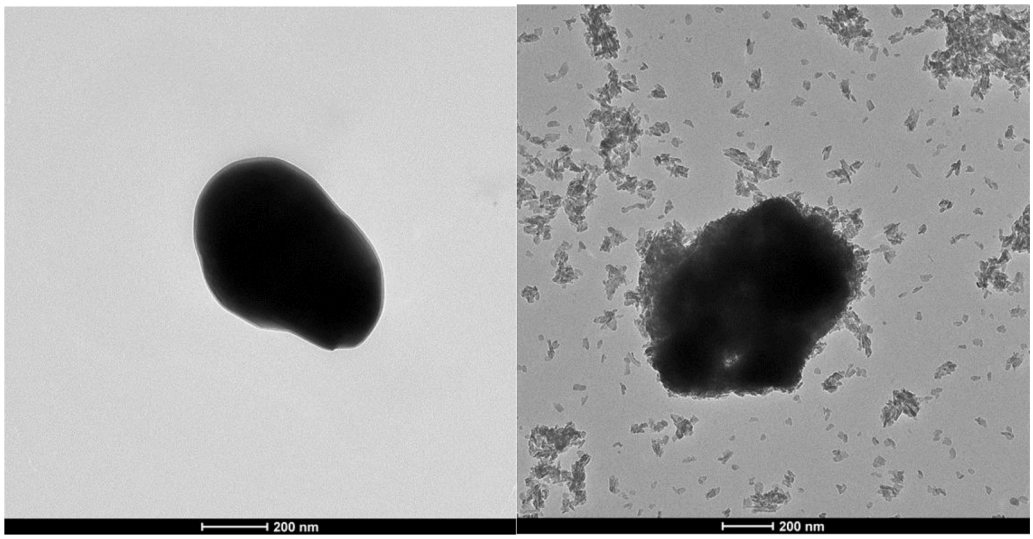


Fig. 12. SEM images of GdB_3O_6 before (left) and after (right) hydroxyapatite coating.

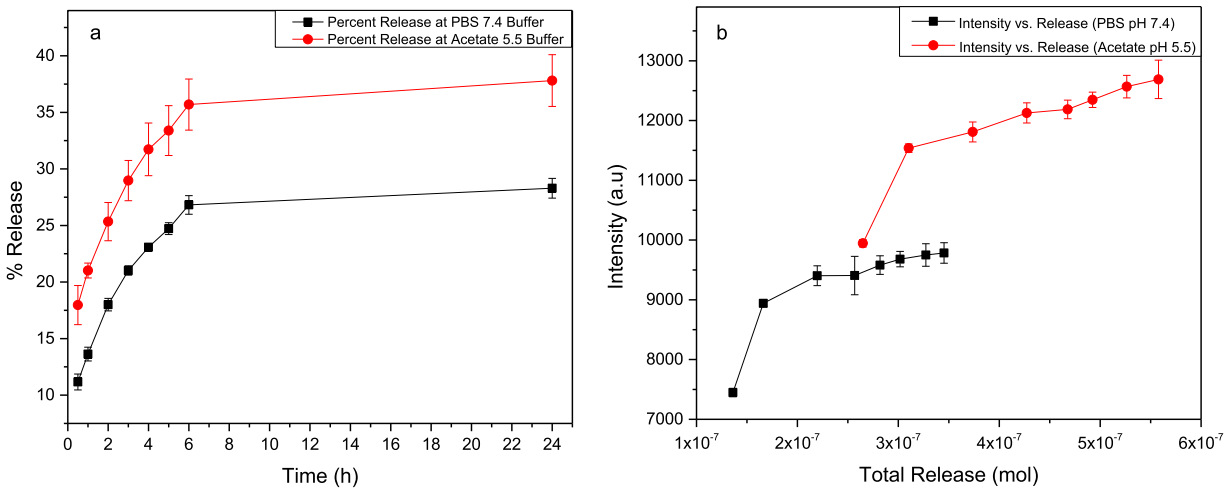


Fig. 13. (a) Percent release at pH 7.4 PBS and 5.5 acetate buffer, (b) Luminescence intensity as a function of total concentration for PBS at pH 7.4 and acetate buffer at pH 5.5.

Photoluminescence measurements for the release of drug from $Gd_{0.825}Eu_{0.175}B_3O_6$@HAP particles were also carried out at pH 5.5 (Fig. 13(b)). The photoluminescence intensity was higher in acetate buffer at pH 5.5 because more moles of the drug was released. The real-time monitoring applications suggested that the intensity of the solution can reflect the release of the drug suggesting that real-time monitoring can be successfully carried out with particles containing a luminescence core.

3.10. Cellular viability

In order to monitor cell viability in the presence of the doxorubicin

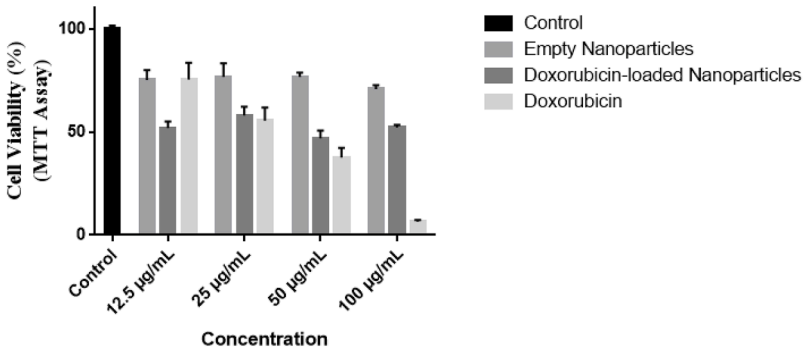


Fig. 14. MTT assay showing the viability of HCT-116 colon cancer cells incubated with doxorubicin loaded $Gd_{0.825}Eu_{0.175}B_3O_6$@HAP@PEG particles.

loaded Gd0.825Eu0.175B3O6@HAP@PEG particles, an MTT assay was carried out with HCT-116 cells (Fig. 14). As a positive control, the cells were also treated with different concentrations of doxorubicin. We observed that $Gd_{0.825}Eu_{0.175}B_3O_6$@HAP particles had low toxicity with nearly 80 % of the cells retaining viability after treatment. HCT116 cells incubated with 12 μg/L $Gd_{0.825}Eu_{0.175}B_3O_6$@HAP particles showed lower viability compared to the same amount of pure doxorubicin with nearly 50 % of the cells killed. Thus, loading of doxorubicin to the particles results in high cell death at low concentrations. Increasing the concentrations of the drug loaded nanoparticle did not lead to any further increase in cell death while pure doxorubicin showed a dose dependent decrease in cell viability, as expected. Albanese et al reported that agglomeration of particles decreased cellular uptake by 25 % compared to monodisperse ones [39], which could be one reason for no further decrease in cell viability with increasing concentration of the particles.

4. Conclusion

Core/shell-type hydroxyapatite particles $Gd_{0.825}Eu_{0.175}B_3O_6$@HAP and Ce^{3+}/Tb^{3+} doped GdB_3O_6 particles were successfully synthesized by the sol-gel process. The sol-gel process for the $Gd_{0.95}Ce_{0.025}Tb_{0.025}B_3O_6$ particle was carried out with citric acid, glycine, tartaric acid, CTAB and EDTA in the core synthesis. The best crystallinity phase and highest luminescence intensity were observed when CTAB was used as a cationic surfactant during the synthesis. Additional $GdBO_3$ phases were found in the GdB_3O_6 structure with citric acid, glycine and tartaric acid chelation. Moreover, the product was found as $GdBO_3$ with EDTA chelation. In the particles doped with different molar ratios of Eu^{3+} ions, an increase in luminescence intensity was observed as the Eu^{3+} ratio was increased. The same experiments were carried out with $GdBO_3$ particles. The highest luminescence intensity was obtained with 17.5 % Eu^{3+} doping for the GdB_3O_6 structure and 20 % Eu^{3+} doping for the $GdBO_3$ structure. According to these results, GdB_3O_6 is a better host than $GdBO_3$ in terms of energy transfer and Eu^{3+} ions emissions which was observed as very high intensity in photoluminescence measurements. Hydroxyapatite was coated on the $Gd_{0.825}Eu_{0.175}B_3O_6$ particles with the wet precipitation method. A decrease in luminescence intensity was observed after the coating due to the absorption of hydroxyapatite at 394 nm. Moreover, the spherical morphology of the $Gd_{0.825}Eu_{0.175}B_3O_6$ particles became uniform sized, granular and well dispersed after hydroxyapatite coating. The same particles were then loaded with doxorubicin and the % drug loading was calculated as 7.82 %. 28 % of the drug was released in 24 h at 37 °C in PBS at pH 7.4, while 40 % of the drug was released when the pH was decreased to 5.5 using acetate buffer. These data suggest that the particles may release the drug more effectively in a tumor microenvironment which is known to have a lower pH. Furthermore, luminescence intensity as a function of total drug release was studied for real-time monitoring. As the drug was released, the luminescence intensity of the particles at 585 nm was increased. Low cell viability was observed with low concentrations of the particle suggesting that high effective cell killing could be observed even with low concentrations of the drug. No further decrease in cell viability was observed with increasing concentration of the particles. Based on the above results, the prepared $Gd_{0.825}Eu_{0.175}B_3O_6$@HAP multifunctional particles can be used as a promising material in the field of biomedical applications.

CRediT authorship contribution statement

Mehmet Burak UZUN: Writing – original draft, Investigation, Formal analysis, Data curation. **İsmail GUDERER:** Methodology, Formal analysis, Data curation. **Sreeparna BANERJEE:** Validation, Methodology, Formal analysis, Data curation. **Ayşen YILMAZ:** Writing – review & editing, Supervision, Project administration, Funding acquisition, Conceptualization.

Declaration of competing interest

The authors declare that they have no known competing financial interests or personal relationships that could have appeared to influence the work reported in this paper.

Data availability

Data will be made available on request.

Acknowledgements

This work was financially supported by TÜBİTAK (Project no: 120Z954) and Middle East Technical University Scientific Research Projects Coordination Unit under grant number TEZ-YL-103–2021–10595, GAP-103–2020–10078.

References

[1] M. Mutailipu, K.R. Poeppelmeier, S. Pan, Borates: a rich source for optical materials, Chem. Rev. 121 (2021) 1130–1202, https://doi.org/10.1021/acs.chemrev.0c00796.
[2] B. Ortega-Berlanga, L. Betancourt-Mendiola, C. Del Angel-Olarte, L. Hernández-Adame, S. Rosales-Mendoza, G. Palestino, An overview of gadolinium-based oxide and oxysulfide particles: synthesis, properties, and biomedical applications, Crystals. (Basel) (2021) 11, https://doi.org/10.3390/cryst11091094.
[3] P. Chanana, A. Uosef, N. Vaughn, M. Suarez-Villagran, R.M. Ghobrial, M. Kloc, J. Wosik, The effect of magnetic field gradient and gadolinium-based MRI contrast agent dotarem on mouse macrophages, Cells 11 (2022), https://doi.org/10.3390/cells11050757.
[4] G.H. Dieke, R.A. Satten, Spectra and energy levels of rare earth ions in crystals, Am. J. Phys. 38 (1970) 399–400, https://doi.org/10.1119/1.1976350.
[5] A. Szczeszak, T. Grzyb, S. Lis, R.J. Wiglusz, Revision of structural properties of GdBO3 nanopowders doped with Eu3+ ions through spectroscopic studies, Dalton Transactions 41 (2012) 5824, https://doi.org/10.1039/c2dt12154a.
[6] H. Zhiran, G. Blasse, Energy transfer phenomena in luminescent materials based on GdB3O6, Mater. Chem. Phys. 12 (1985) 257–274, https://doi.org/10.1016/0254-0584(85)90096-3.
[7] H. Emme, H. Huppertz, High-pressure synthesis of the new rare-earth oxoborate β-Gd2B4O9, Acta Crystallogr. C 61 (2005) i23–i24, https://doi.org/10.1107/S0108270104033396.
[8] P. Akman, S. Ulusan, S. Banerjee, A. Yilmaz, Core/shell type, Ce3+ and Tb3+ doped GdBO3 system: synthesis and Celecoxib drug delivery application, Microporous Mesoporous Mater. 308 (2020) 110528, https://doi.org/10.1016/j.micromeso.2020.110528.
[9] M.P. Chung, Handbook on borates: Chemistry, Production and Applications, 2010.
[10] M.U. Munir, S. Salman, I. Javed, S.N.A. Bukhari, N. Ahmad, N.A. Shad, F. Aziz, Nano-hydroxyapatite as a delivery system: overview and advancements, Artif. Cells Nanomed. Biotechnol. 49 (2021) 717–727, https://doi.org/10.1080/21691401.2021.2016785.
[11] D. Loca, J. Locs, A. Dubnika, V. Zalite, L. Berzina-Cimdina, Porous hydroxyapatite for drug delivery. Hydroxyapatite (Hap) for Biomedical Applications, Woodhead Publishing Series in Biomaterials, Elsevier, 2015, pp. 189–209, https://doi.org/10.1016/b978-1-78242-033-0.00009-2.
[12] J. Fan, S. Wang, W. Sun, S. Guo, Y. Kang, J. Du, X. Peng, Anticancer drug delivery systems based on inorganic nanocarriers with fluorescent tracers, AIChE J. 64 (2018) 835–859, https://doi.org/10.1002/aic.15976.
[13] T. Li, X. Shang, Y. Liu, X. Qiu, Y. Chen, Effects of charges of Eu^{3+}doped LDH laminates on drug loading capacity and drug release as well as its anticancer effects, Research on Chemical Intermediates 50 (2024) 951–972, https://doi.org/10.1007/s11164-023-05185-2.
[14] Y. Liu, T. Li, X. Qiu, X. Shang, Y. Chen, A drug delivery system with fluorescent labeling for the delivery and release of the carboxylate-type camptothecin and its cytotoxicity on HepG2 cancer cell, J. Solgel. Sci. Technol. 108 (2023) 640–654, https://doi.org/10.1007/s10971-023-06218-3.
[15] X. Shang, T. Li, Yi. Liu, X. Qiu, Y. Li, Y. Chen, Fluorescent drug delivery system used for methotrexate and its inhibition against HepG2 cells, J. Iranian Chem. Soc. 21 (2024) 117–127, https://doi.org/10.1007/s13738-023-02910-x.
[16] A.E. Danks, S.R. Hall, Z. Schnepp, The evolution of "sol-gel" chemistry as a technique for materials synthesis, Mater. Horiz. 3 (2016) 91–112, https://doi.org/10.1039/c5mh00260e.
[17] M. Ranjeh, M. Masjedi-Arani, O. Amiri, M. Salavati-Niasari, Pechini sol-gel synthesis of Ni(II) doped LiMnBO3/Li2MnO3/Li2B2O4 nano-photocatalyst under UV–Vis irradiation, Int. J. Hydrogen. Energy 46 (2021) 10324–10336, https://doi.org/10.1016/j.ijhydene.2020.12.149.
[18] C. Zhang, J. Shi, X. Yang, L. De, X. Wang, Effects of calcination temperature and solution pH value on the structural and magnetic properties of Ba2Co2Fe12O22 ferrite via EDTA-complexing process, Mater. Chem. Phys. 123 (2010) 551–556, https://doi.org/10.1016/j.matchemphys.2010.05.013.

[19] T. Tatarchuk, I. Mironyuk, V. Kotsyubynsky, A. Shyichuk, M. Myslin, V. Boychuk, Structure, morphology and adsorption properties of titania shell immobilized onto cobalt ferrite nanoparticle core, J. Mol. Liq. 297 (2020), https://doi.org/10.1016/j.molliq.2019.111757.
[20] S. Leroy, J.F. Blach, A. Kopia, S. Lech, Ł. Cieniek, N. Kania, S. Saitzek, Enhancement of photocatalytic properties of nanosized La2Ti2O7 synthesized by glycine-assisted sol-gel route, J. Photochem. Photobiol. a Chem. 426 (2022), https://doi.org/10.1016/j.jphotochem.2021.113739.
[21] J. Schott, J. Kretzschmar, M. Acker, S. Eidner, M.U. Kumke, B. Drobot, A. Barkleit, S. Taut, V. Brendler, T. Stumpf, Formation of a Eu(iii) borate solid species from a weak Eu(iii) borate complex in aqueous solution, J. Chem. Soc. Dalton Trans. 43 (2014) 11516–11528, https://doi.org/10.1039/c4dt00843j.
[22] M. Seraiche, L. Guerbous, R. Mahiou, A. Potdevin, Synthesis of GdBO3:eu3+ nanophosphors via acetylacetone assisted aqueous sol–gel route: effect of some synthesis parameters, Opt. Mater. (Amst) (2020) 109, https://doi.org/10.1016/j.optmat.2020.110339.
[23] J. Wang, S. Yu, H. Zhang, Effect of surfactants on photoluminescence properties of ZnO synthesized by hydrothermal method, Optik. (Stuttg) 180 (2019) 20–26, https://doi.org/10.1016/j.ijleo.2018.11.062.
[24] F. Meng, X. Zhang, W. Li, T. Xie, H.J. Seo, Luminescence and time-resolved spectroscopy properties of (Gd1-xEux)(BO2)3 multicrystals, J. Phys. Chem. Solids 73 (2012) 564–567, https://doi.org/10.1016/j.jpcs.2011.12.006.
[25] K. Binnemans, Interpretation of europium(III) spectra, Coord. Chem. Rev. 295 (2015) 1–45, https://doi.org/10.1016/j.ccr.2015.02.015.
[26] G. Ju, Y. Hu, L. Chen, X. Wang, Z. Mu, Concentration quenching of persistent luminescence, Physica B Condens. Matter. 415 (2013) 1–4, https://doi.org/10.1016/j.physb.2013.01.027.
[27] R. Li, The Interpretation of UV Absorption of Borate Glasses and Crystals, 1989.
[28] A. Sillen, Y. Engelborghs, The Correct Use of “Average” Fluorescence Parameters, Photochem. Photobiol. 67 (1998) 475–486, https://doi.org/10.1111/j.1751-1097.1998.tb09082.x.
[29] D.V.K. Reddy, S. Taherunnisa, A.L. Prasanna, T.S. Rao, N. Veeraiah, M. Rami Reddy, Enhancement of the red emission of Eu3+ by Bi3+ sensitizers in yttrium alumino bismuth borosilicate glasses, J. Mol. Struct. 1176 (2019) 133–148, https://doi.org/10.1016/j.molstruc.2018.08.057.
[30] R. Singh, A. King, B.B. Nayak, Phase evolution, powder morphology and photoluminescence exploration, of borohydride derived red-emitting Eu3+-doped ZnO nanophosphors, Mater. Sci. Semicond. Process. 133 (2021) 105969, https://doi.org/10.1016/j.mssp.2021.105969.
[31] B.C. Jamalaiah, Optimization of photoluminescence of $GdAl_3(BO_3)_4$:sm^{3+} phosphors for solid state lighting devices, J. Mol. Struct. 1146 (2017) 546–553, https://doi.org/10.1016/j.molstruc.2017.06.033.
[32] C.E. Weir, R.A. Schroeder, Infrared spectra of the crystalline inorganic borates, J. Res. Natl. Bur. Stand. A Phys. Chem. 68A (1964) 467–484, https://doi.org/10.6028/jres.068A.045.
[33] S. Liu, W. Li, S. Dong, S. Gai, Y. Dong, D. Yang, Y. Dai, F. He, P. Yang, Degradable calcium phosphate-coated upconversion nanoparticles for highly efficient chemo-photodynamic therapy, ACS Appl. Mater. Interfaces 11 (2019) 47659–47670, https://doi.org/10.1021/acsami.9b11973.
[34] D.P. Panda, A.K. Singh, T.K. Kundu, A. Sundaresan, $Sc_{1-x}Er_xAlO_3$ perovskites: high-pressure synthesis, photoluminescence properties, and in vitro bioimaging, J. Mater. Chem. C 10 (2022) 16723, https://doi.org/10.1039/d2tc04092a.
[35] A. Langford, T. Horwitz, E. Adu-Gyamfi, C. Wiley, E. Holding, D. Zimmermann, A. A. Ignatius, S. Ohtake, Impact of formulation and suspension properties on redispersion of aluminum-adjuvanted vaccines, J. Pharmaceutical Sci. 109 (4) (2020) 1460–1466, https://doi.org/10.1016/j.xphs.2020.01.006.
[36] H. Zeng, W.R. Lacefield, EDX and XPS, FTIR analysis of pulsed laser deposited calcium phosphate bioceramic coatings: the effects of various process parameters, Biomaterials 21 (2000) 23–30, https://doi.org/10.1016/S0142-9612(99)00128-3.
[37] X. Zhang, Y. Lin, R.J. Gillies, Tumor pH and Its measurement, J. Nucl. Med. 51 (2010) 1167–1170, https://doi.org/10.2967/jnumed.109.068981.
[38] F. Jiang, D.P. Wang, S. Ye, X. Zhao, Strontium-substituted, luminescent and mesoporous hydroxyapatite microspheres for sustained drug release, J. Mater. Sci. Mater. Med. 25 (2014) 391–400, https://doi.org/10.1007/s10856-013-5081-4.
[39] A. Albanese, W.C.W. Chan, Effect of gold nanoparticle aggregation on cell uptake and toxicity, ACS. Nano (2011) 5478–5489, https://doi.org/10.1021/nn2007496.